EasyChair Preprint

№ 13459

Axial Load-Moment Interaction Behavior of Circular FRP-Concrete–Steel Double-Skin Tubular Columns

Fayaz Ahmad Sofi and Vaishnavi Kharate

May 29, 2024

International Conference on Condition Assessment, Rehabilitation & Retrofitting of Structures (CARRS 2023), Department of Civil Engineering, IIT Hyderabad, 10-13 December 2023

AXIAL LOAD-MOMENT INTERACTION BEHAVIOR OF CIRCULAR FRP–CONCRETE–STEEL DOUBLE-SKIN TUBULAR COLUMNS

Fayaz Ahmad Sofi, Ph.D.[1] and Vaishnavi Kharate[2]
[1]*Assistant Professor, Department of Civil Engineering, corresponding author, email: sofifayaz@nitsri.ac.in, National Institute of Technology Srinagar, Jammu and Kashmir – 190006.*
[2]*Former graduate student, Department of Civil Engineering, email: vaishnavikharate05@gmail.com, National Institute of Technology Srinagar, Jammu and Kashmir – 190006.*

ABSTRACT

Double-skin tubular columns (DSTCs) are hybrid columns optimized for a higher strength-to-weight ratio, enhanced ductility, etc., by taking advantage of the mechanical properties of their constituent materials. The confined concrete behavior of DSTCs, having concrete core sandwiched between outer fiber-reinforced polymer (FRP) and inner steel tubes is scantly studied under eccentric compression in the literature. This study investigated the nonlinear behavior of glass FRP-concrete-steel circular DSTCs under eccentric compression loading. A detailed nonlinear finite element modeling was used for generating numerical models after verifying methodology against documented results on tested circular DSTCs for eccentric compression. The compression load eccentricity was varied in numerical models from 0-40 mm, similar to the documented test results. Following numerical model verification, typical five-point axial load-moment interaction curves were developed for the analyzed columns using (1) a theoretical approach based on centrically loaded axial stress-strain formulations for confined concrete, (2) nonlinear finite element analysis methodology, and (3) experimental results. Comparison between theoretical, numerical, and experimental interaction curve results showed close agreements. The research depicted a need for further development of eccentrically loaded axial stress-strain formulations for accurately capturing the axial load-moment interaction behavior of DSTCs.

KEYWORDS

Fiber-reinforced polymer, confined concrete, double-skin tubular columns (DSTCs), nonlinear finite element analysis, eccentric compression.

INTRODUCTION

Confined concrete sandwiched in steel or fiber-reinforced polymer (FRP) single-skin tubes or in double-skin columns between inner and outer tubes have seen potential applications in civil engineering, like modern columns with higher strength-to-weight ratios for high-rise buildings, bridge piers or in retrofitting of existing structures, etc., Ozbakkaloglu et al. (2013) and Joo and Sofi (2023). Compared to traditional reinforced concrete (RC) or steel columns, hybrid FRP-concrete-steel double-skin tubular columns (DSTCs) offer optimized higher load-carrying capacity for lower weights with additional benefits of easily tailorable shapes, enhanced ductility and corrosion resistance in marine environments (Teng et al. 2007; Zakir and Sofi 2022). Teng et al. (2007) first proposed circular-shaped DSTCs at the Hong Kong Polytechnic University and investigated the behavior of these hybrid tubular columns under axial compression. Fig. 1 shows the typical circular shape of hybrid DSTC subjected to concentric compression (Fig. 1a) and eccentric axial loading (Fig. 1b) at eccentricity *e*. The inner steel tube

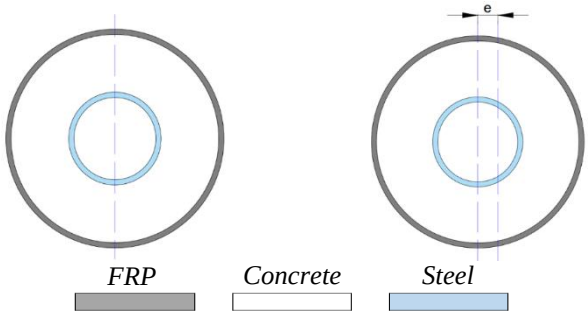

(a) Concentric compression *(b) Eccentric compression*

Figure 1: Hybrid double-skin tubular column (DSTC).

acts as the primary longitudinal reinforcement in DSTCs and prevents concrete spalling (Peng et al. 2018; Sofi et al. 2022a, 2022b). In hybrid DSTCs, the strengths of each material (i.e., FRP, concrete and steel) are optimally utilized to complement the weaknesses of other constituents and achieve the benefits of higher confined concrete strength and improved ductility. The combination of inner and outer tube shapes in DSTCs, such as circle-circle (CC), circle-square (CS), square-square (SS), square-circle (SC), ellipse-ellipse (EE), etc., greatly influence the behavior of confined concrete in DSTCs (Zakir et al. 2021a, 2021b, 2021c).

Most past research on DSTCs focused on tubular column behavior under concentric axial compression, particularly on DSTCs without steel stiffener ribs on the inner tube and referred to as unstiffened DSTCs. Typical concentric failure seen in the constituent materials in unstiffened DSTCs can be attributed to initiation by local buckling deformations of their bare inner steel tubes (Wong et al. 2008; Han et al. 2010; Fanggi and Ozbakkaloglu 2013, 2015; Yu et al. 2017; Zakir and Sofi 2022). Such concentric constituent material failure patterns influence the behavior of DSTCs, including confined concrete strength, axial load-carrying capacity and ductility. In contrast, the DSTCs having inner steel tubes stiffened with vertical steel ribs embedded in confined concrete, referred to as stiffened DSTCs, showed higher axial load-carrying capacity and improved ductility than unstiffened counterparts (Peng et al. 2018; Zakir and Sofi 2022). The stiffened inner steel tubes showed delayed and reduced local buckling deformations and thus improved DSTC behavior. Experimental studies on stiffened DSTCs of different shapes, i.e., CC (Huang et al. 2020; Zakir et al. 2021a; 2021c; Zeng et al. 2021), SC (Peng et al. 2018; Zakir and Sofi 2022) and SS (Zakir et al. 2021b) concluded that presence of stiffened steel tubes improved axial load-carrying capacity and ductility of DSTCs due to enhanced confined concrete axial stress-strain behavior resulting from the delayed, reduced and localized steel tube deformations. Different researchers developed two types of axial stress-axial strain models for confined concrete in DSTCs: (1) design-oriented and (2) analysis-oriented models. The design-oriented formulations are closed-form expressions that can directly evaluate confined concrete stress at any strain, such as the proposed models in Refs. (Ozbakkaloglu et al. 2016; Yu et al. 2010a; Zakir et al. 2021a) for CC shapes and in Refs. (Ozbakkaloglu et al. 2016; Yu and Teng 2013) for SC shaped DSTCs. Yu et al. (2010a) stress-strain model for confined concrete is based on Teng et al. (2009) formulation and provides a void ratio modification factor for CC shapes DSTCs. Teng et al. (2009) model originally applies to FRP-confined concrete without inner void. Ozbakkaloglu et al. (2016) formulation was based on the failure initiation by the inner steel tubes for formulating a confined concrete stress-strain model in CC and SC-shaped DSTCs. Yu and Teng (2013) design-oriented model used the original stress-strain formulations of Lam and Teng (2003) and Teng et al. (2009) for FRP-confined concrete and incorporated void ratio correction in their proposed model applicable to SC-shape, similar correction to that of Yu et al. (2010a) model in CC-shaped DSTCs. Among the numerous iterative analysis-oriented models used in numerical modeling, recent studies (Zakir et al. 2021c; Bhat and Jamatia 2023) proposed formulations for CC, Zakir and Sofi (2022) for SC and Zakir et al. (2021b) for SS-shaped DSTC. Zakir et al. stress-strain formulations apply to confined concrete in stiffened DSTCs.

In reality, columns are generally subjected to eccentric loading (i.e., a combination of axial compression and bending; Fig. 1b) due to (1) unintended factors (e.g., accidental eccentricity in loading, geometric/ material imperfections in the column, etc.), (2) axial compression and end moments and (3) axial compression together with lateral loading (Lin and Teng 2019). Limited research studies have focussed on the behavior of DSTCs for eccentric compression (Fig. 1b). Yu et al. (2010b) experimentally investigated eccentrically loaded hybrid DSTCs and concluded that the FRP confinement effect on concrete behavior lies in between centrically confined (maximum confinement effect) and those loaded in pure bending (having negligible confinement effect). Lin and Teng (2019) proposed an eccentricity-dependent (EccD) stress-strain model that can be used in the layer method of section analysis (theoretical column model using section analysis) for examining more complex confined concrete behavior of eccentrically loaded DSTCs. Gao et al. (2021) experimentally investigated the axial load-moment interaction behavior of reinforced DSTCs by varying eccentricity, void ratio, longitudinal reinforcement ratio, and concrete strength. Eccentricity and void ratio were seen to have an inverse effect on the load-carrying capacity and initial stiffness. Recently, Jiang et al. (2023) and Xie et al. (2023) tested nine large-scale hybrid DSTCs under concentric and eccentric compression loading. Jiang et al. primarily examined the influence of loading eccentricity and FRP tube thickness, whereas Xie et al. varied load eccentricity and slenderness ratio in the test specimens.

The present study builds on the previous research efforts of hybrid DSTCs to examine the axial load-moment interaction behavior of circular hybrid DSTCs subjected to eccentric loading. Typical five-point axial load-moment interaction curves were developed for the analyzed columns using (1) existing theoretical centrically loaded axial stress-strain formulations for confined concrete, (2) nonlinear finite element analysis (NLFEA), and (3) documented experimental results. A detailed nonlinear FE modeling methodology was adopted for generating numerical models after verifying the procedure against documented test results of circular eccentrically loaded DSTCs. A parametric study is in progress for developing an eccentrically loaded stress-strain model for circular DSTCs by varying geometric, material, and loading parameters to examine the influence on their axial load-deformation characteristics and axial load-moment interaction curves.

DOCUMENTED ECCENTRIC COMPRESSION TESTS

The documented test results on five CC-shaped hybrid DSTCs were taken from Gao et al. (2021) and used for numerical model validations in the present study. Table 1 lists the geometric parameters of the outer glass FRP (GFRP) and inner steel tubes, the unconfined compressive strength of concrete (standard cylinder strength) and the eccentricity in the compression loading on tested DSTCs. The test specimen label "GCSEx" represents a hybrid DSTC, where the letters "G", "C", "S" and "E" indicate the outer GFRP tube, concrete sandwiched between tubes, the inner steel tube and eccentric loading on the test specimen, respectively. Single or double-digit Arabic numerals "x" following the letter "E" on the specimen labels represent the specimen number. The specimen GCS0 was tested for concentric axial compression. All test specimens were short columns with a total height (H) of 700 mm, GFRP tube inner diameter ($D_{fi} = D_{co}$) of 200 mm and thickness (t_f) of 5 mm (Fig. 2). The thickness (t_s) of the inner steel tube was fixed at 5 mm, whereas its outer diameter (D_{se}) was varied for different void ratios ($\varphi = D_{se}/D_{fi}$; Table 1). The material properties of the GFRP tube (i.e., hoop directional elastic modulus E_{frp}, hoop tensile strength $f_{h,gfrp}$, and axial compressive strength $f_{z,gfrp}$) are listed in Table 2 (Gao et al. 2021). Similarly, the steel tube material properties (yield stress f_{ys}, ultimate tensile stress f_u, and elastic modulus E_s) obtained from coupon testing are also listed in Table 2.

Table 1: Geometric characteristics of the documented experimental columns.

Specimen Label	Dimensions		FRP Tube		Steel Tube		Eccentricity	Void ratio	Concrete Strength
	D_{fi}	H	D_{fO}	t_f	D_{se}	t_s	e	ϕ	f'_{co}
	(mm)	(mm)	(mm)	(mm)	(mm)	(mm)	(mm)	(%)	(Mpa)
GCS0	200	700	210	5	89	5	0	44.5	44.96
GCSE6	200	700	210	5	89	2	20	44.5	44.96
GCSE8	200	700	210	5	76	5	20	38	44.96
GCSE9	200	700	210	5	108	5	20	54	44.96
GCSE10	200	700	210	5	89	5	40	44.5	44.96

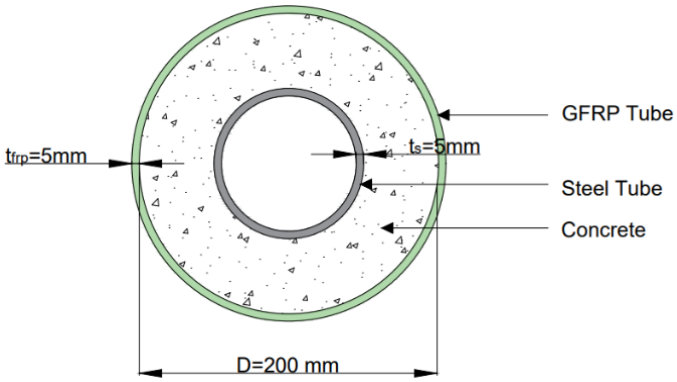

Figure 2: Typical cross-sectinal dimensions of tested DSTC specimens.

Table 2: Material properties of GFRP and steel tubes.

Tube diameter (D_{se} or $D_{fi} = D_{co}$) (mm)	Yield or hoop stress (f_{ys} or $f_{h,gfrp}$) (MPa)	Ultimate stress or compressive strength (f_u or $f_{z,gfrp}$) (MPa)	Elastic modulus (E_s or E_{frp}) (GPa)
Steel tube			
76	254	463	203
89	258	466	200
108	248	461	206
GFRP tube			
200	467	174	27.21

FINITE ELEMENT SIMULATION

Numerical model

In this study, numerical models were generated using ANSYS 2023 commercial software. The nonlinear FE simulations were systematically performed by first developing solid models (i.e., geometry creation) and then converting them to nonlinear FE models using custom-developed ANSYS parametric design language (APDL; ANSYS Inc. 2023a)-based macros, similar to Refs. (Sofi 2017; Sofi and Steelman 2017, 2019, 2021). A consistent and automated numerical model generation procedure was used by custom-developed mapped meshing, defining contact interactions between different components of DSTC columns, nonlinear material modeling, application of eccentric compression loading, post-processing of results, etc. Fig. 3 shows the elements simulating various components of a DSTC. Four node shell elements (Shell 181; ANSYS Inc. 2023b) idealized inner and outer tubes and loading end plates. Mindlin-Reissner's first-order shear-deformation theory governed the behavior of shell elements (theoretical details provided in Kumar et al. 2023). The concrete core was simulated using eight-node solid elements (Solid 185; ANSYS Inc. 2023b). The interaction between GFRP and steel tubes with concrete core was achieved through kinematic relationships between solid and shell elements' degrees of freedom (DOFs). Endplates overlaid with target elements (Targe 170; ANSYS Inc. 2023b) transferred compression loading or reaction through surface-to-surface bonded contact against contact elements (Conta 173) masked on the concrete core. The interaction between endplates and steel tube was idealized by node-to-surface contact, i.e., pairing between target elements of endplates against single-node contact elements (Conta 175) overlaid on tube end cross-sections. Mapped mesh sensitivity from past research (Zakir et al. 2021c; Zakir and Sofi 2022) with an element size of 10 mm for DSTC components and coarse 15 mm for endplates was implemented, which provided consistent matching results against experimental behavior. Displacement-based compression loading was applied on the top endplate nodes falling on a line at eccentricity (e) or all nodes in case of concentric compression along the longitudinal direction of the column (i.e., along - z global coordinate) equal to 1/6th of the column height in multiple nonlinear load steps, whereas the lateral translational DOFs (in $x-$ and $y-$ coordinate directions) of these nodes were restrained. The boundary conditions were applied on the symmetric nodes in the bottom endplate by restraining all three translational DOFs.

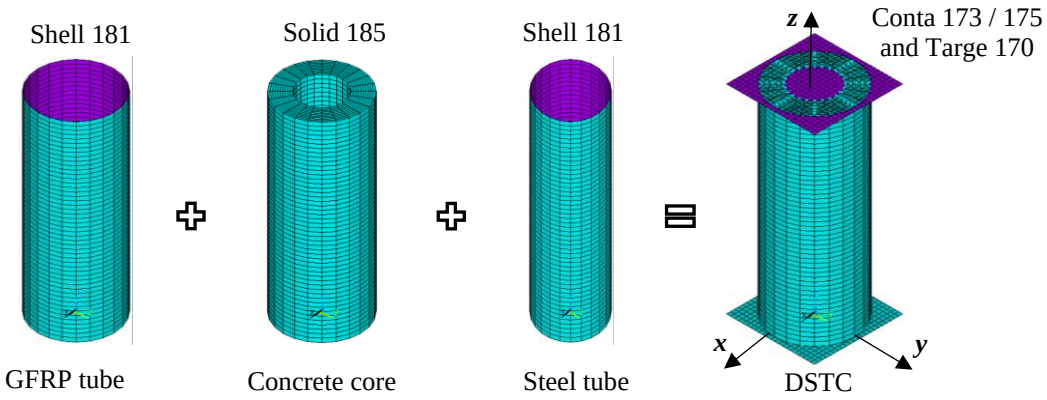

Figure 3: FE modeling of hybrid double-skin tubular column (DSTC).

Constitutive material models

The constitutive behavior of confined concrete, steel and GFRP was simulated in the numerical models using nonlinear material stress-strain curves, plasticity flow rules, and various failure criteria. A three-dimensional (3D) stress state was idealized in confined concrete using the microplane failure theory (ANSYS Inc. 2023b) and isotropic hardening plasticity for the flow rule. Table 3 lists the failure criterion parameters used in the microplane model, similar to Zakir et al. (2021c). Steel plasticity was also assumed with isotropic hardening plasticity with 3D failure based on the von Mises yield criterion. The nonlinear stress-strain curves simulated in the numerical models for concrete, steel and GFRP are briefly described in the following subsections:

Concrete

The points of the passive uniaxial stress (f_c)-strain (ε_c) curve for confined concrete used in FE simulations were iteratively obtained using Eq. (1-6). Eq. (1) was proposed initially by Popovics (1973) and later modified by Mander et al. (1988) for active concrete confinement. The strain (ε_{cc}^*) and corresponding peak confined concrete

stress ($f_{cc}^{\prime *}$) at a specific lateral confining stress (σ_l) can be obtained from Eqs. (2) and (3) of Jiang and Teng (2007), respectively. The increasing confining pressure (σ_l) in FRP-confined concrete for increasing GFRP hoop strain (ε_h), i.e., a passive confinement, can be calculated from Eq. (4) using GFRP material properties from Table 2. The equivalent thickness ($t_{f,eqv.}$) of outer FRP tube in terms of FRP wraps was taken equal to the number of FRP plies multiplied by nominal thickness per ply. The adopted lateral strain (ε_l)-axial strain (ε_c) relationship is given in Eq. (5) and was taken from Jiang and Teng (2007). In the present study, lateral strain (ε_l) was taken equal to and opposite to FRP hoop strain ($-\varepsilon_h$) for strain compatibility. The factor r in Eq. (1) was suggested by Carreira and Chu (1985) and is given by Eq. (6). The elastic modulus (E_c) of unconfined concrete was taken as $E_c = 4730\sqrt{f_{co}^{\prime}}$ (MPa), Jiang and Teng (2007). Unconfined concrete strength ($f_{co}^{\prime}$) was taken from Table 1, and the corresponding strain (ε_{co}) was obtained from $\varepsilon_{co} = 0.000937\sqrt[4]{f_{co}^{\prime}}$ ($f_{co}^{\prime}$ in MPa), unless more accurate test values are available (Popovics 1973).

$$f_c = \frac{f_{cc}^{\prime *}\left(\frac{\varepsilon_c}{\varepsilon_{cc}^*}\right) r}{r - 1 + \left(\frac{\varepsilon_c}{\varepsilon_{cc}^*}\right)^r} \tag{1}$$

$$\frac{\varepsilon_{cc}^*}{\varepsilon_{co}} = 1 + 17.5\left(\frac{\sigma_l}{f_{co}^{\prime}}\right)^{1.2} \tag{2}$$

$$\frac{f_{cc}^{\prime *}}{f_{co}^{\prime}} = 1 + 3.5\frac{\sigma_l}{f_{co}^{\prime}} \tag{3}$$

$$\sigma_l = \frac{2\,E_{frp} t_{f,eqv.} \varepsilon_h}{D_{co}} \tag{4}$$

$$\frac{\varepsilon_c}{\varepsilon_{co}} = 0.85\left(1 + \frac{8\sigma_l}{f_{co}^{\prime}}\right) \times \left\{\left[1 + 0.75\left(\frac{-\varepsilon_l}{\varepsilon_{co}}\right)\right]^{0.7} - e^{-7\left(\frac{-\varepsilon_l}{\varepsilon_{co}}\right)}\right\} \tag{5}$$

$$r = \frac{E_c}{E_c - f_{cc}^{\prime *}/\varepsilon_{cc}^*} \tag{6}$$

Steel

The axial stress (f) at any strain (ε) for steel was assumed as a perfectly elastoplastic curve given by Eq. (7) for the inner tube, where yield stress (f_{ys}) and modulus of elasticity (E_s) correspond to test values (recall Table 2). In this study, Poisson's ratio (ν_s) equal to 0.3 was used in FE simulations. For steel endplates, linear-elastic behavior was assumed with an elastic modulus of 200 GPa.

$$f = \begin{cases} E_s \times \varepsilon & for\ \varepsilon \le \varepsilon_{sy} \\ f_{sy} & for\ \varepsilon > \varepsilon_{sy} \end{cases} \quad ; \text{where, } \varepsilon_{sy} = f_{sy}/E_s \tag{7}$$

GFRP

Glass fibre-reinforced polymer (GFRP) was assumed with transversely isotropic material properties in FE simulations, having an isotropic plane normal to the hoop direction. The simulated GFRP properties are listed in Table 3. Material degradation of fibers and epoxy matrix in FRP tubes was simplified with maximum stress failure criteria in tension and compression, similar to Zakir et al. (2021c). The material property degradation method (MPDG; ANSYS Inc. 2023b) assumed the damage initiation and evolution when stress reduction was upto 70% of the FRP hoop-directional tensile strength and was considered the ultimate state in the numerical models.

Table 3: Microplane failure parameters for concrete and material properties of GFRP used in FE simulations.

Material Type	Microplane material constants (Zakir et al. 2021c)					
	K_0	K_1	K_2	γ_0^{mic}	α^{mic}	β^{mic}
Concrete	0.727	0.727	0.266	0.0000973	0.5	0.3
GFRP (transversely isotropic)	E_x (GPa)	E_y=E_z (GPa)	G_{yz} (GPa)	G_{xy} = G_{xz} (GPa)	μ_{yz}	$\mu_{xy} = \mu_{xz}$
	27.21	3.35	4.34	3.59	0.32	0.27

DISCUSSION OF RESULTS

FE model calibrations

Fig. 4 compares NLFEA versus experimental axial load-deflection characteristics of all five test specimens. Table 4 provides a summary of the plotted results and also compares the moment values at ultimate failure. At the peak stage, axial loads and moment results show excellent agreement between NLFEA vs. experimental values. This can be evidenced by the fact that the average axial load ($P_{p,NLFEA}/P_{p,exp}$) and moment ratios ($M_{p,NLFEA}/M_{p,exp}$) are close to 1.0 (Table 4). The axial load-deflection characteristics showed a disparity in the initial stiffness of columns between NLFEA vs. test results (Fig. 4) for all columns with eccentric loading, which can be attributed to the fact that initial imperfections in the GFRP and steel tubes were not considered in the numerical models. The confined concrete behavior was idealized with a centrically loaded axial stress-strain model, which captured the stiffness of the GCS0 specimen strictly under concentric axial compression (Fig. 4). However, centrically loaded axial stress-strain idealization overestimated the initial stiffness of other DSTC specimens subjected to eccentric compression. The actual FRP confinement effect on concrete lies between centrically confined (maximum confinement effect) and pure bending (negligible confinement effect). The validation study results are of the desired accuracy to capture the hybrid DSTC behavior under eccentric compression loading and can be further used to examine the axial load-moment interaction behavior of circular hybrid DSTCs.

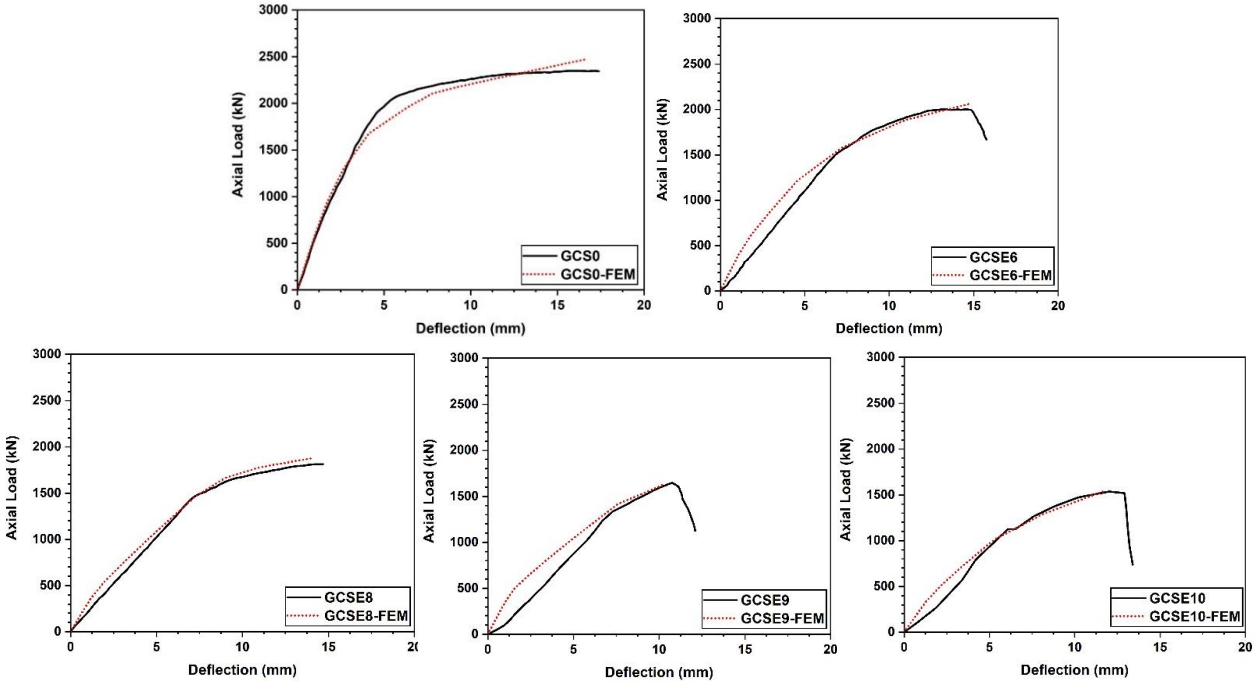

Figure 4: Comparision of NLFEA vs. experimental axial-load deflection characteristics of hybrid DSTCs.

Table 4: Comparison of NLFEA and experimental peak axial loads and moments of tested specimens.

Column label	$P_{p,NLFEA}$ (kN)	$P_{p,exp}$ (kN)	$\frac{P_{p,NLFEA}}{P_{p,exp}}$	$M_{p,NLFEA}$ (kN.m)	$M_{p,exp}$ (kN.m)	$\frac{M_{p,NLFEA}}{M_{p,exp}}$
GCS0	2470	2230	1.11	-	-	-
GCSE6	2067	1996	1.04	41	39	1.05
GCSE8	1882	2038	0.92	38	38	0.98
GCSE9	1632	1647	0.99	33	31	1.05
GCSE10	1549	1553	1.0	62	62	1.0
		Avg. =	1.01			1.02
		St. dev. =	0.07			0.04

Axial load-moment interaction behavior

The axial load (N)-moment (M) curves of the hybrid DSTCs were obtained using (1) the theoretical approach with a centrically loaded axial stress-strain model of Yu et al. (2010a), (2) the nonlinear FE analysis (NLFEA), and (3) documented experimental results. Fig. 5(a) shows a typical $N-M$ interaction curve having five key points (A) to (E) connected by straight lines for various strain distributions in the column cross-section. Point A corresponds to uniform compression strains for zero eccentricity. Point B refers to the neutral axis passing through

the section so that the entire column cross-section experiences compressive strains with almost negligible tension area. Point C is the scenario where the neural axis is tangential to the lowest point of the inner steel tube, and the steel tube is entirely in compression. Point D corresponds to the case of the maximum bending moment capacity of the column cross-section, i.e., the neutral axis coincides with the centroidal line of the column (compression zone height, $X = R$). The final point E, ideally represents the case where the column is under pure bending and has zero axial load capacity. Two cases of strain distribution in the DSTC cross-section can be established (Fig. 5b): (1) compression zone height (X) > section radius (R); and (2) compression zone height (X) ≤ section radius (R). In the theoretical approach, Eqs. (8)-(10) provides the confined concrete stress model of Yu et al. (2010a), which was used for stress analysis for hybrid DSTC cross-sections.

$$f_c = \begin{cases} E_c\varepsilon_c - \dfrac{(E_c - E_{2c})^2}{4f_o}\varepsilon_c^2 & \text{for } \ 0 \le \varepsilon_c < \varepsilon_t \\ f_o + E_{2c}\varepsilon_c & \text{for } \ \varepsilon_t \le \varepsilon_c \le \varepsilon_{cu} \end{cases} \tag{8}$$

$$\frac{f'_{cc}}{f'_{co}} = \begin{cases} 1 + 3.5(\rho_K - 0.01)\rho_\epsilon & \text{if } \rho_K \ge 0.01 \\ 1 & \text{if } \rho_K < 0.01 \end{cases} \tag{9}$$

$$\frac{\varepsilon_{cu}}{\varepsilon_{co}} = 1.75 + 6.5\rho_K^{0.8}\rho_\epsilon^{1.45}(1-\phi)^{-0.22} \tag{10}$$

Based on the stress analysis, the ultimate axial load (N_u) and moment (M_u) can be expressed by Eqs. (11) and (12), respectively:

$$N_u = 0.85f'_{cc}A_{CC} + \sigma_{fc}A_{fc} + f_{ys}(A_{sc} - A_{st}) - \sigma_{ft}A_{ft} \tag{11}$$

$$M_u = 0.85f'_{cc}A_{CC}y_{con} + \sigma_{fc}A_{fc}y_{fc} + f_{ys}(A_{sc}y_{sc} + A_{st}y_{st}) + \sigma_{ft}A_{ft}y_{ft} \tag{12}$$

Where, A_{CC} = cross-sectional area of the compression zone of concrete. A_{fc} and A_{ft} are portions of the sectional areas of the GFRP tube in compression and tension, respectively. Similarly, A_{st} and A_{sc} = portions of sectional area in the steel tube in tension and compression, respectively. The stresses σ_{fc} and σ_{ft} represent the longitudinal direction (axial) compressive and tensile strengths of the GFRP tube material, respectively. Centroidal distances, y_{con}, y_{fc}, y_{ft}, y_{sc} and y_{st}, respectively for sectional areas A_{CC}, A_{fc}, A_{ft}, A_{sc} and A_{st} are calculated using geometric relationships of the cross-section and are provided elsewhere (Gao et al. 2021).

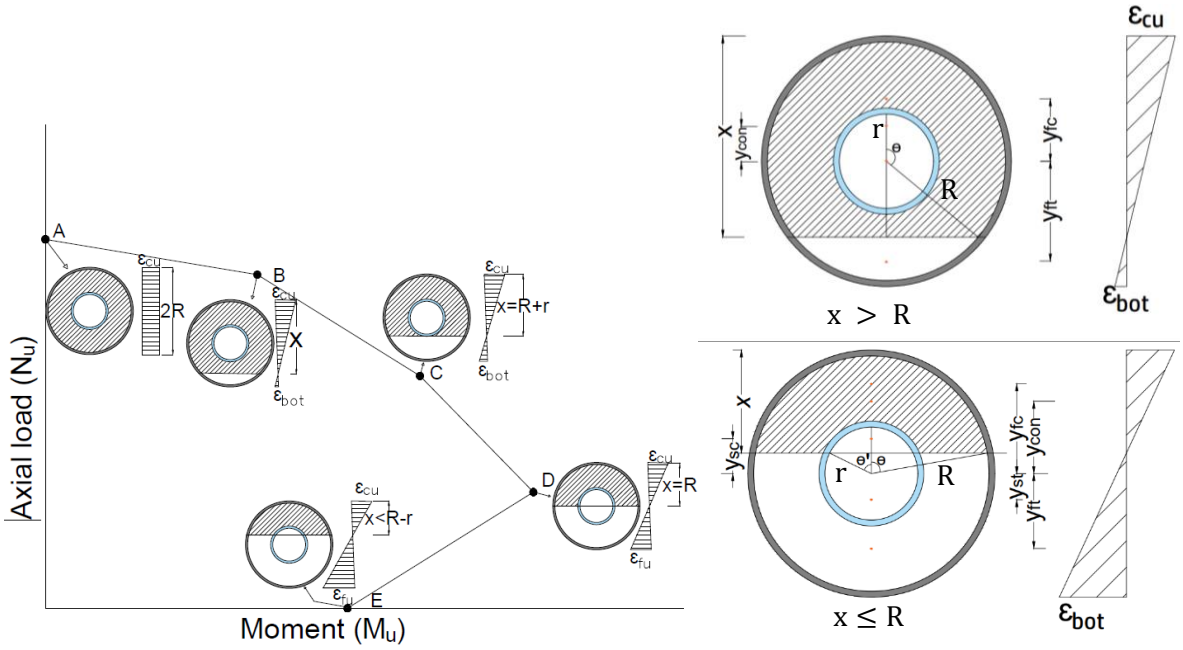

(a) Typical $N - M$ interaction curve *(b) Strain distribution in cross-section*

Figure 5: Typical axial load (N_u)-moment (M_u) interaction behavior of DSTCs.

In the FE approach, Point A was obtained by performing NLFEA under concentric compression for all five DSTC specimens. Point B was obtained by trial and error and was found close to eccentricity (e) equal to 20 mm.

Similarly, Points C and D represented e equal to 40 mm and 100 mm, respectively. Point E was idealized with large eccentricity values, and $e = 125$ mm was used in the present study. All five documented test results of DSTC specimens represented experimental points on respective $N - M(= N.e)$ interaction curves. Fig. 6 compares theoretical, NLFEA-based axial load-moment interaction curves and experimental capacity points (M_u, N_u) for all tested DSTC specimens. It can be seen that specimens GSC0, GCSE6, and GCSE10 (having the same cross-section) with loading eccentricities of 0, 20 and 40 mm, respectively, show excellent agreement between NLFEA-based $N - M$ curve and experimental capacity points (Fig. 6a). The disparity between theoretical and NLFEA results can be attributed to Yu et al. (2010a) centrically loaded axial stress-strain model used in the stress analysis. Similarly, specimens GCSE8 (Fig. 6b) and GCSE9 (Fig. 6c) depicted close agreements between their respective NLFEA-based $N - M$ curves and experimental (M_u, N_u) capacity points, with a slight disparity with the theoretical interaction curve.

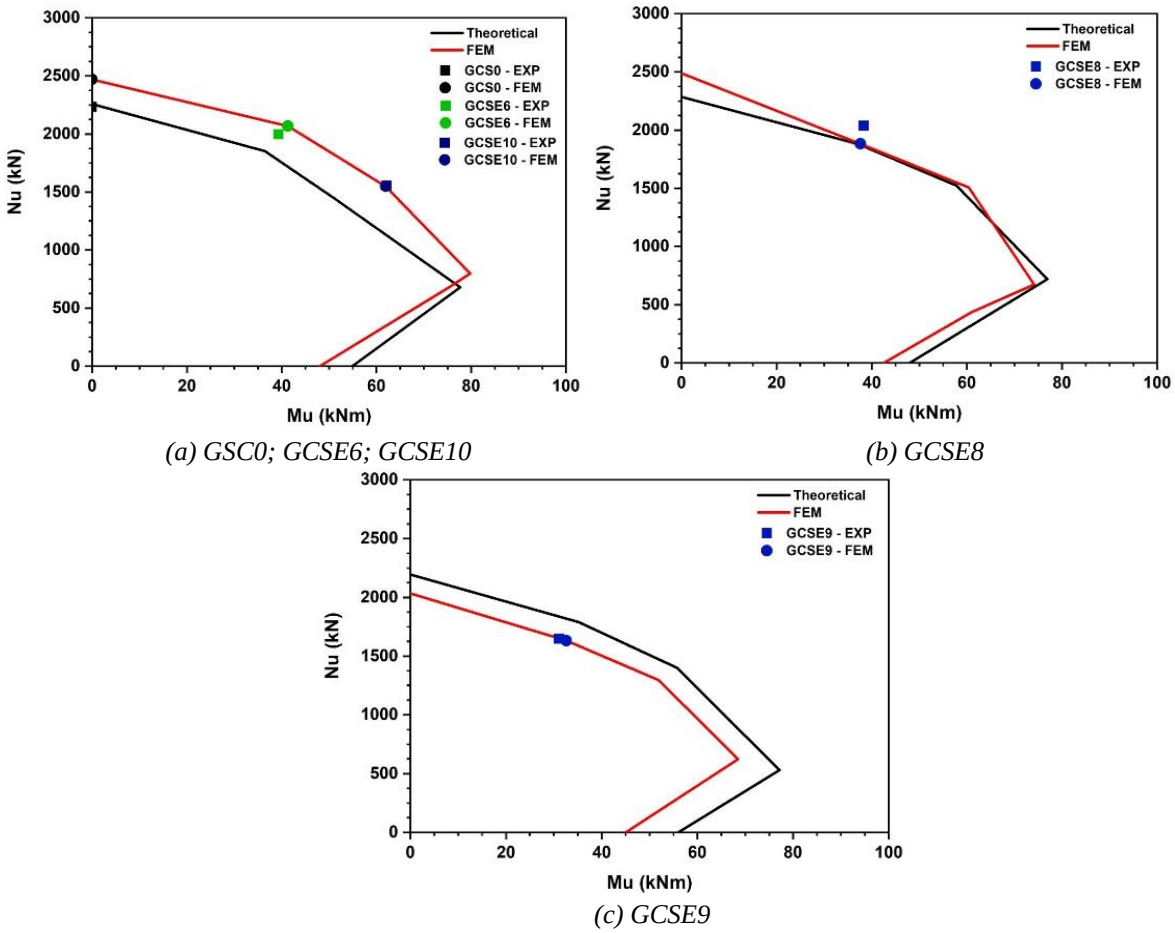

(a) GSC0; GCSE6; GCSE10 *(b) GCSE8*

(c) GCSE9

Figure 6: Comparision of theoretical, numerical and experimental axial load-moment interaction behavior of DSTCs.

CONCLUSIONS

The present study investigated the nonlinear axial load-moment interaction behavior of double-skin glass FRP-concrete-steel circular tubular columns (DSTCs). Five documented DSTC specimens varying in void ratio and compression-loading eccentricity were analyzed using nonlinear finite element methodology. The validation study showed excellent agreement between NLFEA and documented axial load-deformation characteristics. Theoretical and NLFEA-based axial load-moment interaction curves were developed for all DSTC specimens. NLFEA results correlated well with the test axial load-moment capacity points on $N - M$ curve. Theoretical $N - M$ curves showed slight disparity from both NLFEA-based interaction curves and experimental capacity points of DSTC specimens. This evidences a future need to develop more refined eccentrically loaded axial stress-strain models for generating theoretical $N - M$ curves for DSTCs. The need for a new confined concrete stress-strain model can be attributed to the fact that the FRP confinement effect in eccentrically loaded DSTCs lies between centrically confined (maximum confinement effect) and those loaded in pure bending (having negligible confinement effect).

REFERENCES

ANSYS Inc (2023a). Ansys Parametric Design Language Guide. *ANSYS Inc 2023/R2*; Release 2023, 1–106.

ANSYS Inc (2023b). ANSYS Mechanical APDL Element Reference. *ANSYS Inc 2023/R2*; Release 2023, 1–944.

B. Fanggi, T. Ozbakkaloglu (2013). "Compressive behavior of aramid FRP–HSC–steel double-skin tubular columns", *Construction and Building Materials* , 48, 554–65.

B. Fanggi, T. Ozbakkaloglu (2015). "Square FRP–HSC–steel composite columns: Behavior under axial compression", *Engineering Structures*, 92, 156–71.

D. Carreira, K. Chu (1985). "Stress-strain relationship for plain concrete in compression", *ACI Structural Journal*, 82(6), 797–804.

F.A. Sofi (2017). Structural System-based Evaluation of Steel Girder Highway Bridges and Artificial Neural Network (ANN) Implementation for Bridge Asset Management, *Doctoral Dissertation, University of Nebraska-Lincoln*, 1-213.

F.A. Sofi, J.S. Steelman (2017). "Parametric Influence of bearing restraint on nonlinear flexural behavior and ultimate capacity of steel grder bridges", *Journal of Bridge Engineering*, 22(7), 1-18.

F.A. Sofi, J.S. Steelman (2019). "Nonlinear flexural distribution behavior and ultimate system capacity of skewed steel girder bridges", *Engineering Structures*, 197, 1-19.

F.A. Sofi, J.S. Steelman (2021). "Using committees of artificial neural networks with finite element modeling for steel girder bridge load rating estimation", *Structures*, 33, 533–53.

F.A. Sofi, M.R. Joo, R. Seetharaman, M. Zakir (2022a). "Compressive behavior and nonlinear load carrying capacity of multiple-shape concrete-filled double-skin steel tubular columns", *In: Maity, D. et al. Recent Advances in Computational and Experimental Mechanics, Vol—I*, Lecture Notes in Mechanical Engineering, Springer, 473–486.

F.A. Sofi, M. Zakir, J.A. Naqash (2022b). "Experimentally verified behavior of multiple-shape hybrid FRP-concrete-steel double-skin tubular columns under axial compression", *In: Maity, D. et al. Recent Advances in Computational and Experimental Mechanics, Vol—I*, Lecture Notes in Mechanical Engineering, Springer, 167–75.

G. Lin, J.G. Teng (2019). "Stress-strain model for FRP-confined concrete in eccentrically loaded circular columns", *Journal of Composites for Construction*, 23(3), 1-13.

H. Gao, L. Wang, N. Zhang (2021). "Experimental study on FRP–reinforced concrete–steel double-skin tubular columns under eccentric compression loads", *Journal of Composites for Construction*, 25(6), 1-14.

J.G. Teng, T. Jiang, L. Lam, Y.Z. Luo (2009). "Refinement of a design-oriented stress–strain model for FRP-confined concrete", *Journal of Composites for Construction*, 13(4), 269–78.

J.G. Teng, T. Yu, Y.L. Wong, S.L. Dong (2007). "Hybrid FRP–concrete–steel tubular columns: Concept and behavior", *Construction and Building Materials*, 21, 846-54.

J.J. Zeng, Y.Z. Zheng, Y.L. Long (2021). "Axial compressive behavior of FRP-concrete-steel double skin tubular columns with a rib-stiffened Q690 steel tube and ultra-high strength concrete", *Composite Structures*, 268, 1–16.

J. Mander, M. Priestley, R. Park (1988). "Theoretical stress-strain model for confined concrete", *Journal of Structural Engineering*, 114(8), 1804–26.

K. Peng, T. Yu, M. Hadi, L. Huang (2018). "Compressive behavior of hybrid double-skin tubular columns with a rib-stiffened steel inner tube", *Composite Structures*, 204,634–44.

L-H. Han, Z. Tao, F-Y. Liao, Y. Xu (2010). "Tests on cyclic performance of FRP–concrete–steel double-skin tubular columns", *Thin-Walled Structures*, 48, 430–9.

L. Huang, S. Zhang, T. Yu, K.D. Peng (2020). "Circular hybrid double-skin tubular columns with a stiffener-reinforced steel inner tube and a large-rupture-strain FRP outer tube: Compressive behavior", *Thin-Walled Structures*, 155, 1–13.

L. Lam, J.G. Teng (2003). "Design-oriented stress–strain model for FRP-confined concrete", *Construction and Building Materials*, 17(6-7), 471–89.

M.R. Joo, F. A. Sofi (2023). "Unified approach for estimating axial-load capacity of concrete-filled double-skin steel tubular columns of multiple shapes using nonlinear FE models and artificial neural networks", *Practice Periodical on Structural Design and Construction*, 28, 1-27.

M. Zakir, F.A. Sofi (2022). "Experimental and nonlinear FE simulation-based compressive behavior of stiffened FRP-concrete-steel double-skin tubular columns with square outer and circular inner tubes", *Engineering Structures*, 260, 1-18.

M. Zakir, F.A. Sofi, J.A. Naqash. (2021a). "Experimentally verified behavior and confinement model for concrete in circular stiffened FRP-concrete-steel double-skin tubular columns", *Structures*, 34, 1144-57.

M. Zakir, F.A. Sofi, J.A. Naqash. (2021b). "Compressive testing and finite element analysis-based confined concrete model for stiffened square FRP-concrete-steel double-skin tubular columns", *Journal of Building Engineering*, 44, 1-19.

M. Zakir, F.A. Sofi, S. Behera. (2021c). "Nonlinear finite element analysis of circular stiffened FRP-concrete-steel double-skin tubular columns (DSTCs) and experimental compressive behavior of multiple DSTC shapes", *Structures*, 34, 3283–99.

P. Bhat, R. Jamatia. (2023). "Analytical stress-strain model of hybrid FRP-concrete-steel double skin tubular columns under axial compression", *Engineering Structures*, 286, 2–16.

P. Xie, T. Jiang, G. Lin, L. Li, Y. Guo (2023). "Hybrid FRP-concrete-steel double-skin tubular columns of varying slenderness ratios under eccentric compression", *Journal of Constructional Steel Research*, 201, 1-25.

S.A. Kumar, F.A. Sofi, J.A. Bhat (2023). "Equivalent flat-web thicknesses and modified flange-based moment resistance for corrugated-web steel I-girders", *Journal of Constructional Steel Research*, 207, 1–21.

S. Popovics (1973). "A numerical approach to the complete stress-strain relation for concrete", *Cement and Concrete Research*, 3(5), 583–99.

T. Jiang, G. Lin, P. Xie (2023). "Behavior of large-scale hybrid FRP-concrete-steel double-skin tubular columns subjected to eccentric compression", *Engineering Structures*, 275, 1-13.

T. Jiang, J.G. Teng (2007). "Analysis-oriented stress–strain models for FRP–confined concrete", *Engineering Structures*, 29(11), 2968-86.

T. Ozbakkaloglu, B. Fanggi, J. Zheng (2016). "Confinement model for concrete in circular and square FRP–concrete–steel double-skin composite columns", *Materials and Design*, 96, 458–469.

T. Ozbakkaloglu, J. Lim, T. Vincent (2013). "FRP-confined concrete in circular sections: review and assessment of the stress strain models", *Engineering Structures*, 49,1068–88.

T. Yu, J.G. Teng (2013). "Behavior of hybrid FRP-concrete-steel double-skin tubular columns with a square outer tube and a circular inner tube subjected to axial compression", *Journal of Composites for Construction*, 17(2), 271–79.

T. Yu, J.G. Teng, Y.L. Wong (2010a). "Stress-Strain Behavior of concrete in hybrid FRP-concrete-steel double-skin tubular columns", *Journal of Structural Engineering*, 136(4), 379–89.

T. Yu, Y.L. Wong, J.G. Teng (2010b). "Behavior of hybrid FRP-concrete-steel double-skin tubular columns subjected to eccentric compression", *Advances in Structural Engineering*, 13(5), 961–74.

T. Yu, S. Zhang, L. Huang, C. Chan (2017). "Compressive behavior of hybrid double-skin tubular columns with a large rupture strain FRP tube", *Composite Structures*, 171, 10–18.

Y. Wong, T. Yu, J.G. Teng, S.L. Dong (2008). "Behavior of FRP-confined concrete in annular section columns", *Composites Part B: Engineering*, 39, 451–66.